

# Strain-Engineered Anisotropic Optical and Electrical Properties in 2D Chiral-Chain Tellurium

Yixiu Wang, Shukai Yao, Peilin Liao, Shengyu Jin, Qingxiao Wang, Moon J. Kim, Gary J. Cheng, and Wenzhuo Wu\*

Atomically thin materials, leveraging their low-dimensional geometries and superior mechanical properties, are amenable to exquisite strain manipulation with a broad tunability inaccessible to bulk or thin-film materials. Such capability offers unexplored possibilities for probing intriguing physics and materials science in the 2D limit as well as enabling unprecedented device applications. Here, the strain-engineered anisotropic optical and electrical properties in solution-grown, sub-millimeter-size 2D Te are systematically investigated through designing and introducing a controlled buckled geometry in its intriguing chiral-chain lattice. The observed Raman spectra reveal anisotropic lattice vibrations under the corresponding straining conditions. The feasibility of using buckled 2D Te for ultrastretchable strain sensors with a high gauge factor ( $\approx 380$ ) is further explored. 2D Te is an emerging material boasting attractive characteristics for electronics, sensors, quantum devices, and optoelectronics. The results suggest the potential of 2D Te as a promising candidate for designing and implementing flexible and stretchable devices with strain-engineered functionalities.

Atomically thin 2D materials' low-dimensional geometries and superior mechanical properties allow the introduction of enormous strain<sup>[1,2]</sup> (e.g.,  $>1\%$ ) as well as complex, designer


Dr. Y. Wang, Dr. S. Jin, Prof. G. J. Cheng, Prof. W. Wu  
School of Industrial Engineering  
Purdue University  
West Lafayette, IN 47907, USA  
E-mail: wenzhuowu@purdue.edu

Dr. Y. Wang, Dr. S. Jin, Prof. G. J. Cheng, Prof. W. Wu  
Flex Laboratory  
Purdue University  
West Lafayette, IN 47907, USA

S. K. Yao, Prof. P. Liao  
School of Materials Science and Engineering  
Purdue University  
West Lafayette, IN 47907, USA

Dr. Q. Wang, Prof. M. J. Kim  
Department of Materials Science and Engineering  
University of Texas at Dallas  
Richardson, TX 75080, USA

Prof. W. Wu  
Birck Nanotechnology Center  
Purdue University  
West Lafayette, IN 47907, USA

 The ORCID identification number(s) for the author(s) of this article can be found under <https://doi.org/10.1002/adma.202002342>.

DOI: 10.1002/adma.202002342

strain fields<sup>[3–5]</sup> without fracture. These materials are amenable to exquisite mechanical manipulation<sup>[6,7]</sup> with a broad tunability inaccessible to bulk or thin-film materials.<sup>[8,9,4]</sup> Such capability offers unexplored possibilities for probing intriguing physics and materials science in the 2D limit due to the strong coupling of mechanical strain to various internal degrees of freedom involving charges, photons, and spins for engineering novel functionalities.<sup>[10–13]</sup> Recently, strain engineering in 2D semiconductors, such as transition metal dichalcogenides<sup>[14–18]</sup> and black phosphorus<sup>[19–22]</sup> has been explored theoretically<sup>[20,23,24]</sup> and experimentally as an effective approach to rationally manipulate the atomic structure, lattice vibration, electronic and optical properties, and device performance of related materials.<sup>[9,6,25–27,24]</sup>

Lattice structure and crystal symmetry dictate a 2D semiconductor's properties and their interaction with the external stimuli.<sup>[28,29,2,30,31]</sup> Many 2D materials with reduced symmetry (e.g., BP,<sup>[32]</sup> ReS<sub>2</sub>,<sup>[28]</sup> Ta<sub>2</sub>NiS<sub>5</sub>,<sup>[33]</sup> etc.) show strong in-plane anisotropy, leading to significant differences in property change and material response when the strain is applied along different in-plane crystalline directions.<sup>[28,29,34,2,31]</sup> Exploration of the anisotropic strain response and properties in 2D materials has both scientific (e.g., anisotropic plasmons, linear dichroism, etc.)<sup>[35,36]</sup> and technologic significance (e.g., polarization-sensitive detectors,<sup>[37,38,36,39]</sup> polarized imaging devices,<sup>[40,29]</sup> and high-performance multiaxial strain sensors).<sup>[28]</sup>

2D tellurium (Te), an emerging 2D semiconductor,<sup>[41]</sup> boasts attractive characteristics, such as high carrier mobility, large electro-optic activity, superior air-stability, strong spin-orbit interaction, chirality-induced Weyl nodes, etc.<sup>[42–44,38,45,41,46,47]</sup> 2D Te's intriguing structure<sup>[48,45,41,49]</sup> consists of an anisotropic chiral-chain crystal lattice. Each Te atom is covalently bonded with its two nearest neighbors on the same chain, and the inter-chain interaction is weaker than the covalent bond.<sup>[50]</sup> A systematic study on the impact of strain engineering on the 2D Te's anisotropic properties will be helpful for both deepening the fundamental understanding of this new material and designing as well as developing more capable device applications.

Herein, we systematically investigated the strain-engineered anisotropic electrical and optical properties in 2D Te, through

designing and introducing a controlled buckled geometry in solution-grown large area 2D Te crystal. The wavelength and amplitude of the buckled geometry, as well as the local strain, were characterized by experimental and theoretical studies. The observed Raman spectra from the chiral-chain lattice of 2D Te, dependent on the magnitude and orientation of the applied strains, reveals the anisotropic lattice vibration response under the corresponding straining conditions. We further explored the feasibility of using buckled 2D Te for ultrastretchable strain sensors with a high gauge factor ( $\approx 380$ ). Our results suggest the potential of 2D Te as a promising candidate for designing and implementing flexible electronics,<sup>[51–53]</sup> wearable sensors,<sup>[54,55]</sup> and deformable optoelectronics.<sup>[56–58]</sup> The experimental platform can also enable the exquisite mechanical control in 2D Te and other 2D materials with substrate-induced, on-demand, controlled strains.

Tellurium (Te) hosts a unique chiral-chain structure different from the lattices of the widely studied 2D layered materials<sup>[59,60]</sup> (Figure 1a.). The helical chains, stacked through a weak interaction,<sup>[50,61]</sup> consist of covalently bonded Te atoms and exhibit a three-fold screw symmetry along the [0001] direction.<sup>[62]</sup> The high-resolution transmission electron microscopy (TEM) results in Figure 1b resolves such characteristic helical-chain lattice of our solution-grown 2D Te, which naturally exhibits geometric anisotropy with the long, straight edge always parallel to the [0001] direction<sup>[45,41,49]</sup> (Figure 1c). Such geometric anisotropy facilitates the rapid determination of lattice orientations without using sophisticated approaches (e.g., second-harmonic generation<sup>[13]</sup>

or reflectance difference microscopy<sup>[63]</sup>) that are usually required for studying other 2D materials.

It should be noted, though, our previous synthesis protocol produces trapezoid shape 2D Te with large length (i.e., the straight edge along [0001] direction can reach 100–300  $\mu\text{m}$ ) much larger than the width (i.e., the length along  $[\bar{1}2\bar{1}0]$  direction is around 5–15  $\mu\text{m}$ ). To facilitate the fundamental exploration of the anisotropic properties (e.g., mechanical, electrical, etc.) along the main in-plane directions (i.e., [0001] and  $[\bar{1}2\bar{1}0]$ ) in 2D Te, it would be desirable to synthesize 2D Te flakes with larger widths. To this end, we leverage our previous findings<sup>[45,41]</sup> for modulating the dimension and improving the productivity/yield through controlling growth kinetics and thermodynamics in the synthesis process. Details for the modified synthesis process can be found in the Experimental Section. Briefly, the dimensions and yield of 2D Te flakes were controlled by unraveling the fundamental coupling between three critical synthetic parameters: reaction time, precursor concentration, and pH value of the reaction solution. Our results show that a morphology evolution with time from 1D structures to 2D forms, similar to our previous report,<sup>[45]</sup> occurs for all the processes (Figure 1d–f; and Figures S1–S3, Supporting Information). The flakes produced from 20 h reactions are much wider than those derived from the 10 h reactions. When the synthesis time increases to 30 h, the average widths for the 2D Te flakes are similar to those from the 20 h reactions, likely due to the saturated 2D Te crystallization with the consumption of the Te salt<sup>[41]</sup> (Figures S1–S3, Supporting Information). Another important

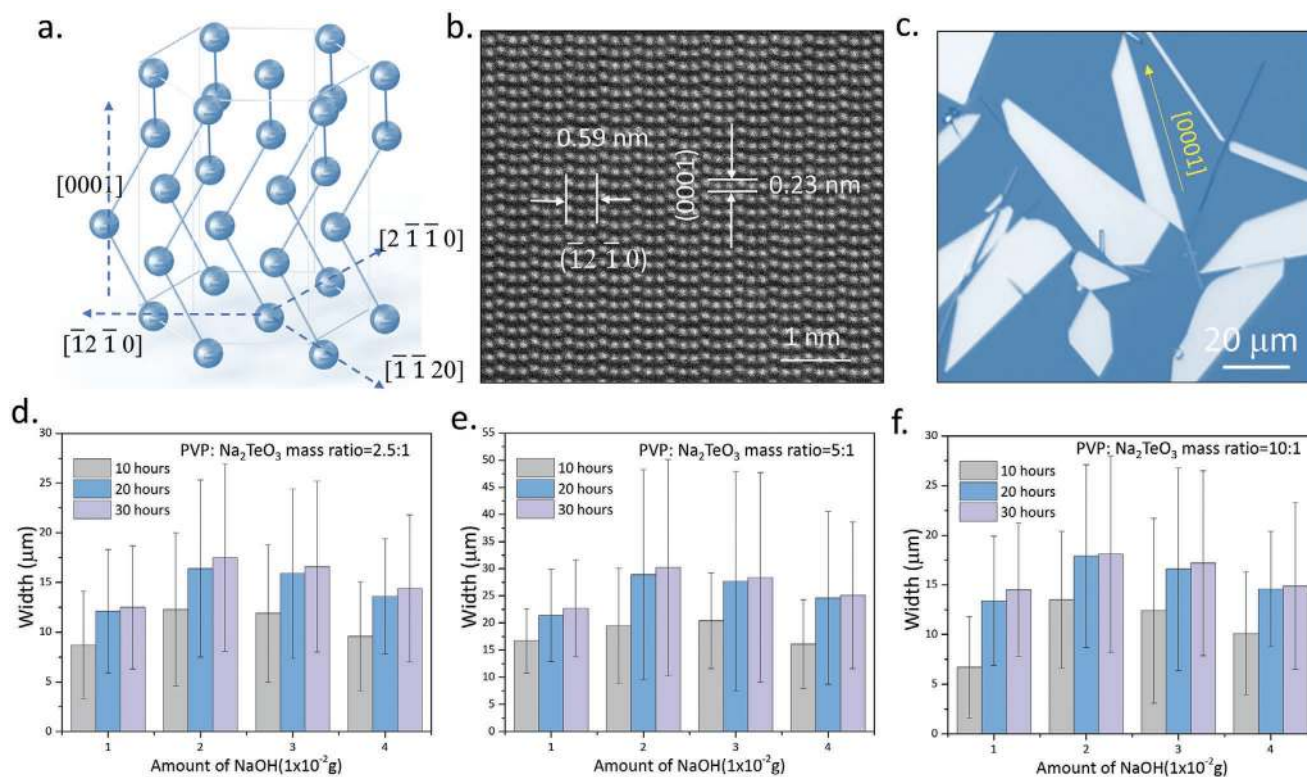


**Figure 1.** Characterization of 2D Te. a) The crystal structure of tellurium. b) High-resolution transmission electron microscopy image of 2D Te. c) Optical microscopy image of 2D Te. d–f) Width modulation for 2D Te. The average values from 8 technical replicates are indicated, and error bars represent one standard deviation for each set of replicates.

synthesis parameter is the mass ratio between the precursors (poly(vinylpyrrolidone) (PVP) and  $\text{Na}_2\text{TeO}_3$ ). As shown in Figure 1d,f, when we kept constant the growth time and the amount of NaOH, an intermediate mass ratio (5:1, Figure 1e) leads to a larger average width compared to the other two groups where low and high mass ratios are used. As is shown in Figure 1e, when 0.02 g NaOH is mixed in the solution, the width of the resultant flakes can reach 50  $\mu\text{m}$ , which is among the highest value for the reported solution-growth 2D materials.<sup>[64–66]</sup> Figure S2 (Supporting Information) shows that these Te flakes have widths ranging from 20 to 50  $\mu\text{m}$  and length up to 100  $\mu\text{m}$ , which significantly facilitates the subsequent device fabrication and characterization along different crystal directions. The dependence of the width modulation on the mass ratio could be understood by examining the different surface energies of the Te crystal structure, as well as the different PVP capping effects on the Te crystal surfaces.<sup>[45,41]</sup> When a small amount of PVP is used (Figure 1d), the homogeneous nucleation of Te can occur without sufficient passivation, consuming resources for subsequent growth. Ostwald ripening of the Te nuclei is consequently short, which leads to the smaller flake sizes than samples that were grown with higher PVP concentration (Figure 1f). However, when a higher PVP concentration is used, the excessive passivation of the Te crystal facets with PVP

limits the crystal growth process. Additionally, we found that the pH value of the reaction solution also affects the width control. The results in Figure 1d suggest that when the pH of the reaction solution is  $\approx 10$ –11 (when 0.02–0.03 g NaOH is added), the obtained 2D Te flakes possess the largest widths. The same trend can also be observed when the mass ratio between PVP and  $\text{Na}_2\text{TeO}_3$  is 2.5: 1 and 10:1, respectively (Figure 1e,f). For the nucleation and growth of Te crystal in alkaline media, it has been reported that the reaction rate would decrease with the increased concentration of NaOH<sup>[41]</sup> (Supporting Equations). The lower reaction rate in the solution with higher NaOH concentration is thought to be responsible for the formation of seeds with larger dimensions.<sup>[67]</sup> After the Ostwald ripening, the larger seeds lead to the larger crystal size. Moreover, our previous work revealed the inhomogeneous growth of 2D Te with a suitable amount of PVP capping agent.<sup>[41]</sup> These processes collectively lead to the observed large 2D Te flakes in the reaction with higher NaOH concentration. Meanwhile, It has been reported that Te will react with NaOH when the concentration of NaOH is excessive.<sup>[68]</sup> Therefore, the dissolution of Te in NaOH leads to 2D Te with small width with an excess amount of NaOH.

The fabrication process of buckled 2D Te is depicted in Figure 2a. First, poly(dimethylsiloxane) (PDMS) substrate was stretched with a controlled prestrain (the Experimental Section).

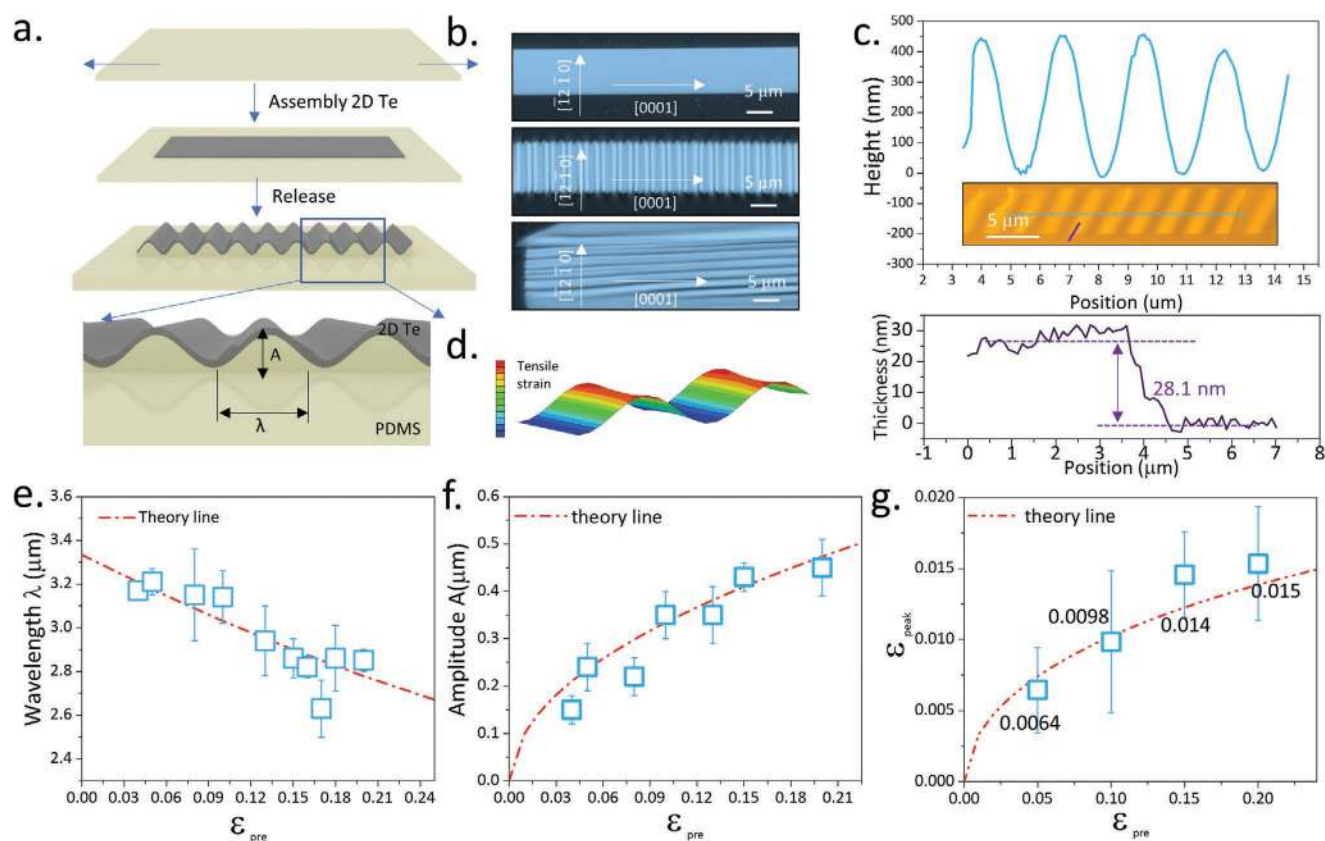


**Figure 2.** Fabrication and topography characterization of buckled 2D Te. a) Schematic procedure of fabricating the 2D wavy geometry on PDMS. b) Optical microscopy image of the 2D Te without buckling and with buckling along different directions. c) Atomic force microscopy (AFM) image of the wavy 2D Te. d) Abaqus calculation results of the strain distribution on buckling 2D Te. The colored bar on the left-hand side indicates the intensity of the strain. e–g) The wavelength, amplitude, and peak strain of the buckling 2D Te with different prestrain. The average values from 5 technical replicates are indicated, and error bars represent one standard deviation for each set of replicates.

Then, the as-synthesized 2D Te was transferred on the PDMS by a Langmuir–Blodgett (LB) method.<sup>[45,41]</sup> After the prestrain was released, a periodic “wavy” topography was formed along the stretching direction.<sup>[3,6]</sup> As is shown in Figure 2a,  $\lambda$  and  $A$  represent the wavelength and amplitude for the wrinkle, respectively. Additionally, the “wavy” direction can be crumpled along different crystal directions through the orientation-deterministic transfer of the 2D Te crystals on the prestrained substrates (Figure 2b). With controlled prestrain direction, the 2D Te flake can be buckled along [0001] and  $[\bar{1}2\bar{1}0]$  directions. Contact-mode atomic force microscopy (AFM) was used to probe the wavelength, amplitude, and thickness of the buckled 2D Te. The inset in Figure 2c shows the AFM result of the buckled 2D Te on a PDMS substrate with a 20% prestrain. Typical AFM results for samples with different prestrain values are shown in Figure S4 (Supporting Information). The line-scan results show that this buckled 2D Te (from the 20% prestrain substrate) has a wavelength of 3  $\mu\text{m}$ , an amplitude of 0.55  $\mu\text{m}$ , and a thickness of 28.1 nm. Using these measured parameters, we have simulated the strain distribution in this wavy 2D Te using finite-element-method (Abaqus). The analysis in Figure S5 (Supporting Information) indicates that the shear force at the interface between PDMS and 2D Te confines the 2D Te in the wavy buckled shape. Such shearing force results in the shift of the neutral mechanical plane toward the bottom of the 2D Te film near the crest region and toward the top of the 2D Te film near the valley region (Figure S5, Supporting Information). As a result, the tensile regions along the entire buckled 2D Te are larger than the compress regions (Figure S5, Supporting Information), and the peak strain locates at the crest regions of the buckled flake (Figure 2d). As shown in Figure 2c, the buckled configuration can be modeled using a nonlinear finite deformation theory model.<sup>[6,4]</sup> Figure 2e,f depicts the detailed quantitative profile of the 2D Te in the wavy configuration. A general comparison of the flakes withstanding different prestrain values shows that the wavelength decreases from 3.2 to 2.8  $\mu\text{m}$ . In comparison, the amplitude increases from 0.15 to 0.4  $\mu\text{m}$  when the prestrain is increased from 5% to 20% (indicated by the open squares in Figure 2e,f). Here, the elastomeric PDMS substrate undergoes a significant strain and can be modeled as a Neo-Hookean solid using the 2nd Kirchhoff stress formation.<sup>[25,69]</sup> Through energy minimization, the final buckled configuration can be modeled using a cosine function as per the finite deformation mechanics theory.<sup>[6,69]</sup> The profile of the buckled 2D Te structure can then be described by amplitude and wavelength as<sup>[70,6,4,69]</sup>

$$\lambda = \frac{\lambda_0}{(1 + \epsilon_{\text{pre}})(1 + \xi)^{1/3}}, A = \frac{A_0}{\sqrt{1 + \epsilon_{\text{pre}}}(1 + \xi)^{1/3}} \quad (1)$$

$$\text{where } A_0 = h \sqrt{\frac{\epsilon_{\text{pre}}}{\epsilon_c} - 1}, \lambda_0 = 2\pi h \left(\frac{\bar{E}_f}{3\bar{E}_s}\right)^{1/3}, \epsilon_c = \frac{1}{4} \left(\frac{3\bar{E}_s}{\bar{E}_f}\right)^{2/3}, \xi = 5\epsilon_{\text{pre}}(1 + \epsilon_{\text{pre}})/32, h$$

is the thickness of 2D Te,  $\epsilon_{\text{pre}}$  is the prestrain,  $\bar{E}_f$  and  $\bar{E}_s$  represent the plane strain modulus of 2D Te and substrate, respectively. The Young's modulus and Poisson's ratio of the PDMS substrate are  $E_s = 2$  MPa and  $\nu_s = 0.5$ , which are dependent on the curing process.<sup>[71,72]</sup> As is discussed in the previous work,<sup>[73]</sup> the  $\bar{E}_f$  and  $\bar{E}_s$  is rather insensitive to small variation of Poisson's ratio between nanomaterials and its bulk status, so

the Poisson's ratio value  $\nu_f = 0.33$  of bulk tellurium given in the literature<sup>[74]</sup> is applied here. Equation (1) indicates that we can derive Young's modulus of 2D Te flakes from the relationship between the buckling wavelength  $\lambda$  and the flake thickness  $h$ . To this end, we used three different flakes with 28.1, 26.2, 35.7 nm thickness, and determined Young's moduli of the flakes are 50.74, 43.45, and 48.02 GPa, respectively (Table S1, Supporting Information), which shows slightly higher value than buck Te (40 GPa).<sup>[75]</sup> The model represented by Equation (1) has been plotted in Figure 2e,f (dashed lines), which fit well with the experimental data. The peak strain induced in the buckled 2D Te can then be expressed by

$$\epsilon_{\text{peak}} = 2\sqrt{\epsilon_{\text{pre}}\epsilon_c} \frac{(1 + \xi)^{1/3}}{\sqrt{1 + \epsilon_{\text{pre}}}} \quad (2)$$

which is determined by the prestrain  $\epsilon_{\text{pre}}$  and  $\epsilon_c$ , the critical buckling strain which is given by  $\epsilon_c = \frac{1}{4} \left(\frac{3\bar{E}_s}{\bar{E}_f}\right)^{2/3}$ . Here the above-determined Young's modulus (50.74 GPa for 28.1 nm thick Te flake) is used here. The resultant relationship between  $\epsilon_{\text{peak}}$  and  $\epsilon_{\text{pre}}$  is depicted by the dashed line in Figure 2g. Meanwhile, we can also experimentally evaluate the peak strain induced in the buckled 2D Te flakes, based on the measured AFM topography images (e.g., Figure 2c) and the following expression (see the Experimental Section)

$$\epsilon_{\text{2D Te}}^{\text{peak}} = \frac{\pi^2 Ah}{\lambda^2} \quad (3)$$

where  $h$  is the thickness of 2D Te. Using the measured amplitude ( $A$ ) and wavelength ( $\lambda$ ), we determine that the peak strain is 0.64%, 0.98%, 1.45%, and 1.53% when 5%, 10%, 15%, and 20% prestrains were applied (Figure 2g). These experimentally determined values also fall close to the theoretically predicted curve (Figure 2g).

We next characterized the anisotropic optical properties of the strained 2D Te with Raman spectroscopy at room temperature (see the Experimental Section). Raman spectroscopy (Figure S6, Supporting Information) has been widely adopted to probe the surface vibrational modes and image the strain distribution in 2D materials.<sup>[14,9,76]</sup> The Raman spectra in Figure 3a shows the two main Raman-active modes locating at 118.9  $\text{cm}^{-1}$  ( $A^1$ -mode), and 138.8  $\text{cm}^{-1}$  ( $E^2$ -mode) for a 28 nm thick unbuckled flat 2D Te flake. These two peak positions are slightly smaller than those from strain-free 2D Te flakes with similar thickness.<sup>[77–80]</sup> Such a slight shift for the  $A^1$ -mode and  $E^2$ -mode peaks is likely due to the existence of residual stress introduced from the transfer<sup>[81]</sup> and LB assembly<sup>[82–84]</sup> processes. In our experiment, we maintain the same parameters for all transfer and LB assembly steps. The  $A^1$ -mode peak located at 118.9  $\text{cm}^{-1}$  corresponds to the chain expansion in the basal plane vertically to [0001] helical chain. The  $E^2$ -mode peak locates at 138.8  $\text{cm}^{-1}$  is caused by the asymmetric stretching along the [0001] helical chain<sup>[45,41]</sup> (Figure 3b). In our work, the incident laser light impinges vertically onto the substrate, and we obtain the peak frequency of each mode by Lorentz function fitting. Figure 3c shows the optical image of the buckled 28 nm thick Te flake with a 20% prestrain. The area highlighted with green dashed

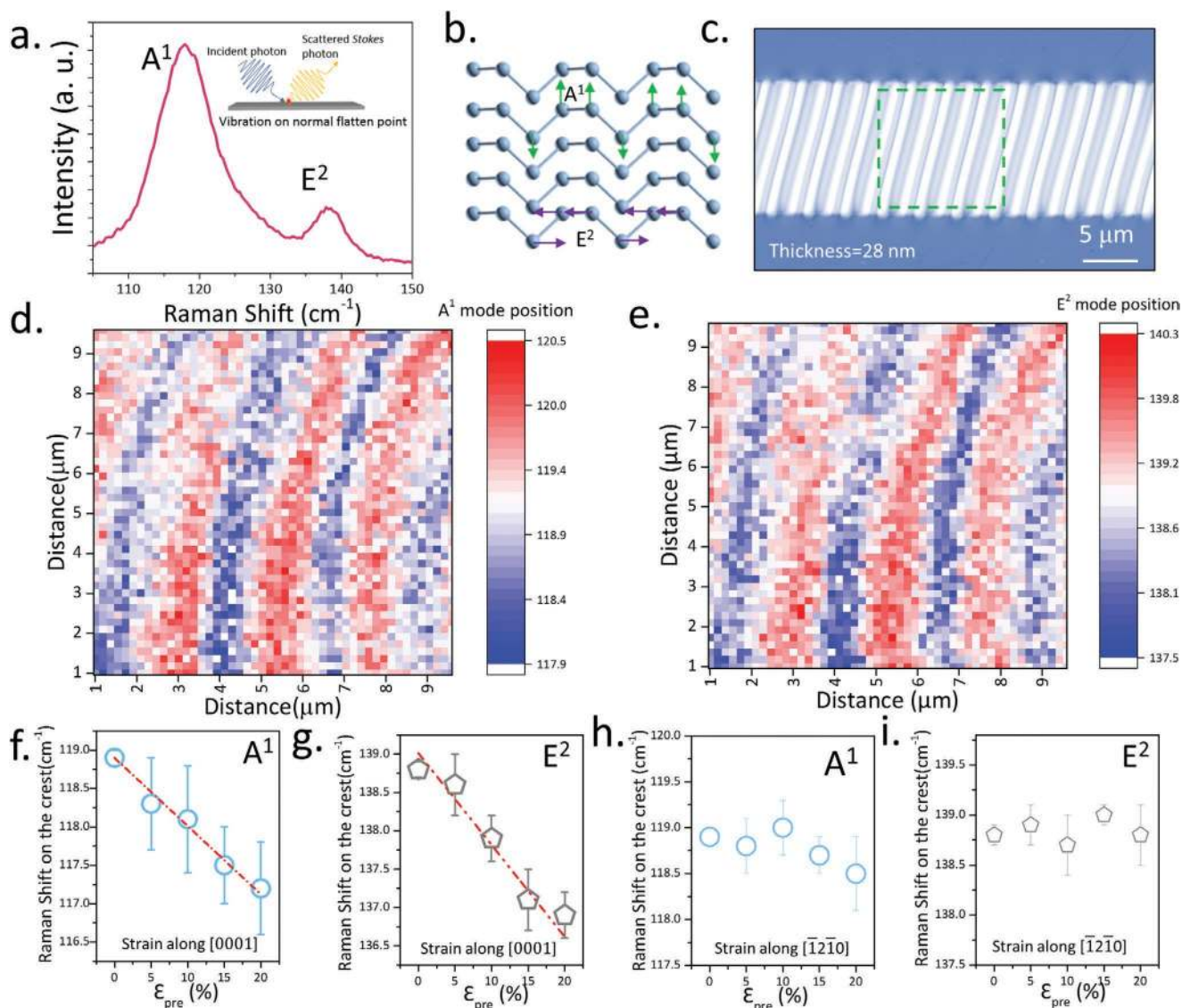


**Figure 3.** Anisotropic optical property of the buckled 2D Te. a) Typical Raman spectra of the 2D Te crystal. b) Schematic shows the main Raman-active modes in 2D Te. c) Optical image of the buckled 2D Te. d,e) Scanning Raman spectroscopy maps plotting of the A<sup>1</sup> and E<sup>2</sup> mode peak frequencies. f,g) The Raman shift of the A<sup>1</sup> and E<sup>2</sup> modes under [0001] direction strain. h,i) Raman shifts of the A<sup>1</sup> and E<sup>2</sup> modes under  $\bar{1}\bar{2}\bar{1}0$  direction strain. The average values from 3 technical replicates are indicated, and error bars represent one standard deviation for each set of replicates.

lines ( $10 \times 10 \mu\text{m}^2$ ) was selected for the scanning Raman spectra mapping with  $1 \mu\text{m}$  resolution. The resultant mapping for the Raman shift for A<sup>1</sup> and E<sup>2</sup> modes are shown in Figure 3d,e, respectively. These contour plots show that the periodically varying strain is consistent over the entire wavy geometry in Figure 3c. The red region (higher frequency than the original peaks in Figure 3a) and the blue area (lower frequency than the original peaks in Figure 3a) in Figure 3d,e indicate that uniaxial tensile and compressive strains are induced at the valley and the crest regions of the buckled 2D Te, which is consistent with our previous study.<sup>[43]</sup> We can also observe in Figure 3d,e, the gradual decrease of the frequency from the crest toward the valley regions, which manifests the strain distribution in the entire area. On the other hand, the scanning Raman spectra mapping for 2D Te under  $\bar{1}\bar{2}\bar{1}0$  direction strain has also been

performed (Figure S7, Supporting Information). We found that  $\bar{1}\bar{2}\bar{1}0$  strain hardly introduces the periodical Raman shift as is in the case for the [0001] strain.

Next, we conducted a quantitative analysis for the Raman spectra shift of buckled 2D Te (Figure S8, Supporting Information). As is shown in Figure 3f,g, the two modes show redshift with increased prestrains in the substrate. For A<sup>1</sup>-mode, the Raman frequency shifts  $1.7 \text{ cm}^{-1}$  when 20% prestrain was applied. The slope of the shift is  $\approx 1.1\%$  under uniaxial tensile strains along the [0001] direction (Figure 3f). The E<sup>2</sup>-mode has a redshift with a slope of 1.2% under uniaxial tensile strains (Figure 3g). As a comparison, we examined the Raman shift when the prestrain was applied along the  $\bar{1}\bar{2}\bar{1}0$  direction. Different from the Raman response in [0001] direction, both A<sup>1</sup> and E<sup>2</sup> modes have shown no apparent Raman shift even the

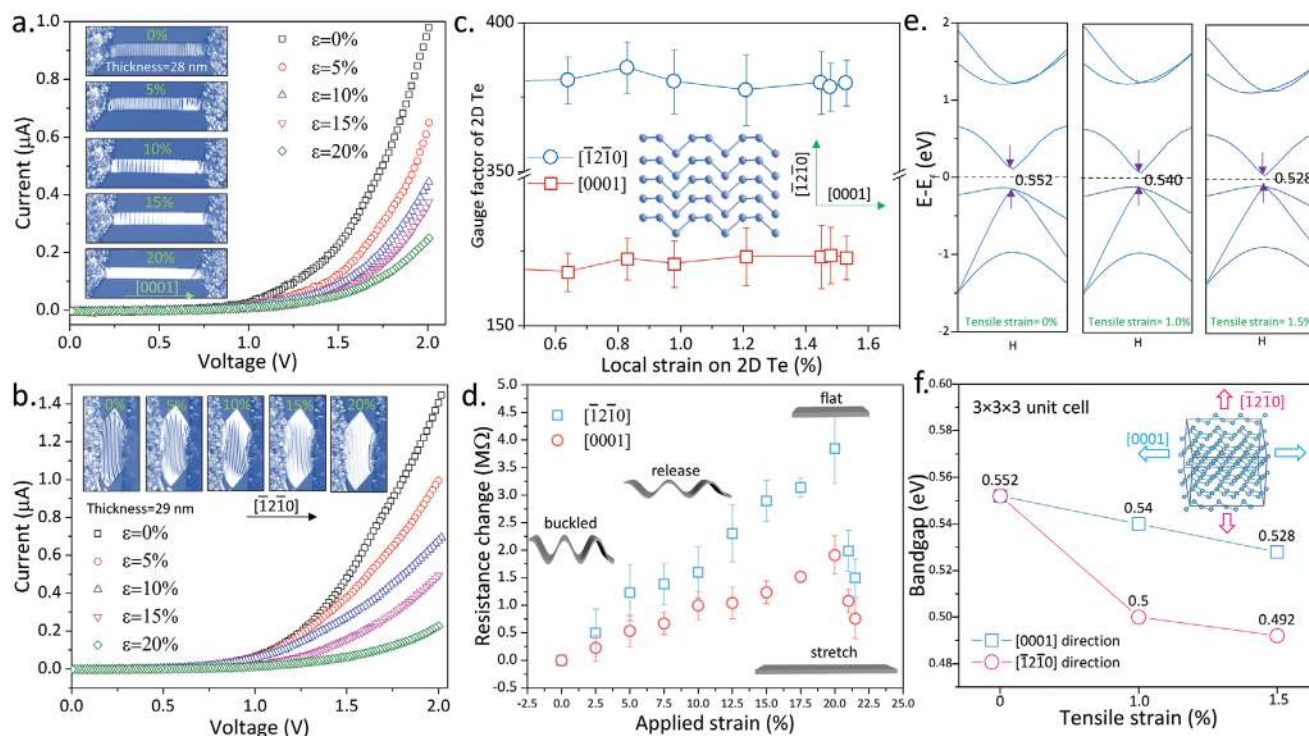


**Figure 4.** Anisotropic electrical property and strain-sensing capability of the buckled 2D Te. a) The current–voltage curve of the 2D Te with buckling in [0001] direction. b) The current–voltage curve of the 2D Te with buckling in  $[\bar{1}2\bar{1}0]$  direction. c) The gauge factor of the 2D Te strain sensor with buckling and straining in [0001] and  $[\bar{1}2\bar{1}0]$  direction, respectively. d) The resistance change value when the as-fabricated sensor experiences the applied strain from 2.5% to 21.5%. e, f) Calculation results of the bandgap change when the tensile strain is applied.

prestrain was increased to 20%. (Figure 3h,i), which is similar to the previous work.<sup>[43]</sup> The different responses in the Raman spectra when prestrains were applied along different directions can be understood by examining the intrinsic vibration modes and the electro-optic interactions in Te. When the prestrain was applied along the [0001] direction, tensile, and compressive strains were induced along the [0001] direction in the crest and valley regions, respectively, of the buckled 2D Te. As a result, the Te–Te covalent bond at the surface of 2D-Te was elongated (at the crest) or shortened (at the valley) along the [0001] direction, which weakens or enhances the interatomic interaction.<sup>[85,32,86]</sup> The asymmetric stretching of Te atoms along the [0001] helical chain direction hence became softening or hardening, leading to the decreased (at the crest) or increased (at the valley) vibration frequency of  $E^2$  mode, which has also been observed in other 2D materials.<sup>[87,76]</sup> Meanwhile, this softening (or hardening) effect introduce weaker(or stronger) Te atoms oscillating perpendicular to the basal plane, which is similar to other 2D materials,<sup>[14]</sup> resulting in a decreased (or increased) vibration frequency of the Te helical chain expansion, which is associated with the  $A^1$  mode.<sup>[88]</sup> On the other hand, the inter-chain interaction (along  $[\bar{1}2\bar{1}0]$  directions) is weaker than covalent bond.<sup>[62]</sup> When the prestrain was applied along the  $[\bar{1}2\bar{1}0]$  direction, tensile, and compressive strains were induced along the  $[\bar{1}2\bar{1}0]$  direction in the crest and valley regions, respectively, of the buckled 2D Te. However, the absence of covalent bond along the  $[\bar{1}2\bar{1}0]$  direction<sup>[61]</sup> and larger space (the intrachain between neighboring Te atoms is 0.29 nm, while the interchain

distance is 0.35 nm) along this direction makes the external strain to be released without significant bond and bond angle change compared to the [0001] case (see our density functional theory (DFT) calculation results in Table S2, Supporting Information). Moreover, it has been revealed by the previous literature<sup>[89]</sup> that the optical activity along [0001] direction is higher than that in the  $[\bar{1}2\bar{1}0]$  direction in tellurium. Consequently, the  $A1$  and  $E2$  vibration mode hardly show Raman response along the  $[\bar{1}2\bar{1}0]$  direction.

We further investigated the anisotropic strain-engineered electrical transport along different directions in buckled 2D Te (Figure 4). To this end, we fabricated a stretchable two-terminal strain sensor based on a single buckled 2D Te with source and drain electrodes, all fabricated on a prestrained PDMS substrate (Figure 4a). As is shown in Figure 4a inset, the 2D Te strain sensor with a 20% prestrain can withstand tensile strains up to 20%. On the contrary, the 2D Te flake transferred to an unstrained PDMS substrate was permanently destroyed when the tensile strain was applied up to 20% (Figure S9, Supporting Information). During the strain-engineered electrical transport measurement (Figure 4), the current–voltage ( $I$ – $V$ ) curves from the 2D Te device was recorded as the released PDMS substrate was uniaxially stretched. The strain values shown in Figure 4 indicate such applied strains ( $\epsilon$  in Figure 4). As is shown in Figure 4a inset, the buckling morphology in the 2D Te (thickness 28 nm, Figure S10, Supporting Information) decreases with the increased applied strain. When a 20% strain was applied, the 2D Te was stretched back to the flat shape

(Figure 4a). The  $I$ - $V$  characteristics of the device under different strains along [0001] direction is shown in Figure 4a. The source-drain current ( $I_{ds}$ ) was measured with a fixed source voltage from 0 to 2 V. It can be seen that  $I_{ds}$  decreases from  $9.8 \times 10^{-7}$  to  $2.5 \times 10^{-7}$  A ( $V_d = 2$  V) when the applied strain increases from 0% to 20%. We also performed similar characterization for devices fabricated with 2D Te flakes where the buckling is formed along  $[\bar{1}\bar{2}\bar{1}0]$  direction (Figure 4b inset, the flake thickness is 29 nm (Figure S10, Supporting Information)). The  $I$ - $V$  characteristics of such devices under different strains along  $[\bar{1}\bar{2}\bar{1}0]$  direction are shown in Figure 4b. We found that the drain current decreases from  $1.4 \times 10^{-6}$  to  $2.3 \times 10^{-7}$  A with the applied substrate strain increases from 0% to 20% (Figure 4b). To evaluate and compare the strain effect on modulating the electrical transport in Figure 4a,b, we plotted the corresponding gauge factors (GF) for both cases (Figure 4c). GF is a widely used figure of merit for evaluating the sensitivity of strain sensors, which relates the change in electrical resistance to the applied strain,<sup>[90]</sup> through

$$GF = (\Delta R/R)/\varepsilon \quad (4)$$

where  $\Delta R/R$  is the normalized change in the measured electrical resistance, and  $\varepsilon$  is the applied strain. In the calculation, we derived the channel resistance (excluding the Schottky contacts) of the 2D Te devices by fitting the measured  $I$ - $V$  characteristics, following the reported approaches.<sup>[91]</sup> The gauge factors of the buckled 2D Te for each direction with different strains are summarized in Figure 4c. We could derive the local strain on the 2D Te crystal by  $\varepsilon_{2D\text{Te}}^{\text{peak}} = \frac{\pi^2 Ah}{\lambda^2}$  as we mentioned before. Combined with the resistance change, we plotted the GF of the 2D Te with local strain in Figure 4c. The GF in  $[\bar{1}\bar{2}\bar{1}0]$  can be up to 380, which shows high sensitivity for strain sensor application (Table S3, Supporting Information). Furthermore, we extracted the resistance change (the difference of current resistance and the initial resistance, resistance change =  $R_x - R_0$ ) as a function of strain (Figure 4d). It is evident that the resistance change in  $[\bar{1}\bar{2}\bar{1}0]$  direction is more substantial than that in [0001] direction. After the applied strain exceeds 20%, the resistance changes for both directions start to decrease (Figure 4d). This phenomenon is due to the strain-induced bandgap change. As we discussed previously, tensile strained regions (the crest areas) dominate in the buckled 2D Te when the applied substrate strain ( $\varepsilon$  in Figure 4) is low (e.g., < 20%). Our simulation results (Figure 4e) suggest that tensile strains reduce the bandgap of 2D Te and thus make the device more conductive than the ones made with unbuckled flake 2D Te flakes due to the piezoresistance effect.<sup>[28,55]</sup> Meanwhile, the increased applied strain on the device reduces the buckling amplitude and local tensile strains experienced by the 2D Te in the crest regions. The continuously-decreased local tensile strains lead to the increased resistance observed in Figure 4d. After the applied strain exceeds 20%, the flat 2D Te starts to experience a global tensile strain within the flake, which contributes to the observed resistance reduction (for strains larger than 20%) in Figure 4e; and Figure S11 (Supporting Information). To understand the observed difference in GF for different crystal directions, we employed DFT (see the Experimental Section) to calculate the bandgap change

in different crystal directions. As is shown in Figure 4f, when 0% tensile strain was applied, bandgap in both directions show the same value of 0.55 eV. As the tensile strain increases to 1.0%, the bandgap decreases to 0.54 eV for tensile strain along the [0001] direction, while the bandgap decreases to 0.50 eV for tensile strain along the  $[\bar{1}\bar{2}\bar{1}0]$  direction. With the tensile strain increases to 1.5%, the bandgap for Te under strain along the [0001] and  $[\bar{1}\bar{2}\bar{1}0]$  directions become 0.53 and 0.49 eV, respectively. Such orientation-dependent and strain-induced bandgap change also contributes to the observed anisotropic GF and strain responses in Figure 4c.

In summary, we systematically investigated the strain-engineered anisotropic electrical and optical properties in 2D Te, through applying a facile buckling strategy to solution-grown large area 2D Te crystal. The observed Raman spectra from the chiral-chain lattice of 2D Te reveals the anisotropic lattice vibration under the corresponding straining conditions. We further explored the feasibility of using buckled 2D Te for ultrastretchable strain sensors with a high gauge factor. Our results suggest the potential of 2D Te as a promising candidate for designing and implementing flexible and wearable functional devices.

## Experimental Section

**Synthesis of 2D Te:** The synthesis of high-quality 2D Te has previously been described. In the typical hydrothermal synthesis, 0.101 g of  $\text{Na}_2\text{TeO}_3$  and 0.5 g of PVP ( $M_w = 55\,000$ ) were put into a Teflon-lined stainless-steel autoclave and dissolved in double-distilled water under vigorous magnetic stirring to form a homogeneous solution at room temperature. After that, hydrazine hydrate and NaOH were added sequentially into the mixed solution under vigorous magnetic stirring. The container was closed and maintained at 180 °C for 30 h. Then, the autoclave was cooled naturally to room temperature.

**LB Transfer of 2D Te:** The 2D Te nanoflake monolayers can be transferred to PDMS substrates by the LB technique. The washed 2D Te were mixed with *N,N*-dimethylformamide (DMF), and  $\text{CHCl}_3$ . Then the above solution was dropped into the deionized water. After 30 min, the monolayer 2D Te can be transferred to any substrates.

**Localization Strain Calculation by the Thin-Film Geometry:** The shape of the wavy 2D Te could be expressed by a simple sine function,  $y = (A/2) \cdot \sin(kx)$  ( $k = 2\pi/\lambda$ ). The peak strain occurs at the peaks of the waves can be calculated using  $\varepsilon_{2D\text{Te}}^{\text{peak}} = \frac{h}{2R_c}$ , where  $h$  is the 2D Te thickness, and  $R_c$  is the radius of curvature at the peak, which is given by  $R_c = -\frac{1}{y''} \Big|_{x=\pm \frac{(2n-1)\pi}{2k}}$  where  $n$  is an integer and  $y''$  is the second derivative of  $y$  with respect to  $x$ . Then the peak strain can be expressed by  $\varepsilon_{2D\text{Te}}^{\text{peak}} = \frac{\pi^2 Ah}{\lambda^2}$ .

**Raman Spectra:** Angle-resolved Raman spectra were measured at room temperature. Raman signal was excited by 633 nm He-Ne laser. The incident light comes in along  $[\bar{1}\bar{0}\bar{1}0]$  direction, which is perpendicular to the Te flake. A linear polarizer was placed in front of the spectrometer to polarize reflected light in the same direction with incident light.

**DFT Calculation:** Electronic structure and phonon properties calculations are performed using the augmented projector wave method<sup>[92]</sup> implemented in the Vienna Ab initio Simulation Package (VASP) version 5.4.4.<sup>[93,94]</sup> OptPBE-vdW was chosen to be the exchange and correlation functional.<sup>[95]</sup> To fully optimize the structure, the cutoff energy of plane wave was 400 eV, and a  $5 \times 5 \times 3$  Gamma-centered k-point grid was taken to sample the first Brillouin zone. The force convergence setting was taken to be 0.01 eV Å<sup>-1</sup> on each atom. The electronic wavefunction

convergence criterion is  $10^{-8}$  eV. A 3-atom hexagonal unit cell was used for model Te crystal.

## Supporting Information

Supporting Information is available from the Wiley Online Library or from the author.

## Acknowledgements

W.Z.W. acknowledges the College of Engineering and School of Industrial Engineering at Purdue University for the startup support and the Ravi and Eleanor Talwar Rising Star Assistant Professorship. The synthesis, optical, and electrical characterization of 2D Te and related devices were partially sponsored by the National Science Foundation under Grant No. CMMI-1762698. The strain engineering experiments were supported by a seed grant from the Purdue College of Engineering EFC Future of Manufacturing program. The computational research was supported in part through computational resources provided by the Information Technology department at Purdue University, West Lafayette, IN, USA. G.J.C. acknowledges the support from the National Science Foundation under Grant No. CMMI-1538360.

## Conflict of Interest

The authors declare no conflict of interest.

## Author Contributions

W.Z.W. conceived and supervised the project. W.Z.W. and Y.X.W. designed the experiments. Y.X.W. synthesized the materials, fabricated the devices, and characterized the samples. S.Y.J. and G.J.C. characterized the strained samples with Raman spectra. S.K.Y. carried out the first-principles calculations under the supervision of P.L.L., Q.X.W., and M.J.K. performed the TEM characterization. W.Z.W. and Y.X.W. analyzed the data and wrote the manuscript. All authors have discussed the results and commented on the paper.

## Keywords

2D tellurium, anisotropy, strain engineering

Received: April 5, 2020

Revised: May 7, 2020

Published online:

- [1] G. H. Ahn, M. Amani, H. Rasool, D.-H. Lien, J. P. Mastandrea, J. W. Ager III, M. Dubey, D. C. Chrzan, A. M. Minor, A. Javey, *Nat. Commun.* **2017**, *8*, 608.
- [2] J. Tao, W. Shen, S. Wu, L. Liu, Z. Feng, C. Wang, C. Hu, P. Yao, H. Zhang, W. Pang, X. Duan, J. Liu, C. Zhou, D. Zhang, *ACS Nano* **2015**, *9*, 11362.
- [3] W. Bao, F. Miao, Z. Chen, H. Zhang, W. Jang, C. Dames, C. N. Lau, *Nat. Nanotechnol.* **2009**, *4*, 562.
- [4] D.-Y. Khang, H. Jiang, Y. Huang, A. Rogers, *Science* **2006**, *311*, 208.
- [5] J. Zang, S. Ryu, N. Pugno, Q. Wang, Q. Tu, M. J. Buehler, X. Zhao, *Nat. Mater.* **2013**, *12*, 321.
- [6] H. Jiang, D.-Y. Khang, J. Song, Y. Sun, Y. Huang, J. A. Rogers, *Proc. Natl. Acad. Sci. USA* **2007**, *104*, 15607.
- [7] Y. Sun, W. M. Choi, H. Jiang, Y. Y. Huang, J. A. Rogers, *Nat. Nanotechnol.* **2006**, *1*, 201.
- [8] J. Cao, E. Ertekin, V. Srinivasan, W. Fan, S. Huang, H. Zheng, J. W. L. Yim, D. R. Khanal, D. F. Ogletree, J. C. Grossman, J. Wu, *Nat. Nanotechnol.* **2009**, *4*, 732.
- [9] S. Deng, A. V. Sumant, V. Berry, *Nano Today* **2018**, *22*, 14.
- [10] J. Feng, X. Qian, C.-W. Huang, J. Li, *Nat. Photonics* **2012**, *6*, 866.
- [11] H. Li, A. W. Contryman, X. Qian, S. M. Ardakani, Y. Gong, X. Wang, J. M. Weisse, C. H. Lee, J. Zhao, P. M. Ajayan, J. Li, H. C. Manoharan, X. Zheng, *Nat. Commun.* **2015**, *6*, 7381.
- [12] D. Voiry, H. Yamaguchi, J. Li, R. Silva, D. C. B. Alves, T. Fujita, M. Chen, T. Asefa, V. B. Shenoy, G. Eda, M. Chhowalla, *Nat. Mater.* **2013**, *12*, 850.
- [13] W. Wu, L. Wang, Y. Li, F. Zhang, L. Lin, S. Niu, D. Chenet, X. Zhang, Y. Hao, T. F. Heinz, J. Hone, Z. L. Wang, *Nature* **2014**, *514*, 470.
- [14] A. Castellanos-Gomez, R. Roldán, E. Cappelluti, M. Buscema, F. Guinea, H. S. J. van der Zant, G. A. Steele, *Nano Lett.* **2013**, *13*, 5361.
- [15] D. Lloyd, X. Liu, J. W. Christopher, L. Cantley, A. Wadehra, B. L. Kim, B. B. Goldberg, A. K. Swan, J. S. Bunch, *Nano Lett.* **2016**, *16*, 5836.
- [16] S. Manzeli, A. Allain, A. Ghadimi, A. Kis, *Nano Lett.* **2015**, *15*, 5330.
- [17] E. Scalise, M. Houssa, G. Pourtois, V. Afanas'ev, A. Stesmans, *Nano Res.* **2012**, *5*, 43.
- [18] S. Wagner, C. Yim, N. McEvoy, S. Kataria, V. Yokaribas, A. Kuc, S. Pindl, C.-P. Fritzen, T. Heine, G. S. Duesberg, M. C. Lemme, *Nano Lett.* **2018**, *18*, 3738.
- [19] M. A. Bissett, M. Tsuji, H. Ago, *Phys. Chem. Chem. Phys.* **2014**, *16*, 11124.
- [20] W. Gaoxue, G. C. Loh, P. Ravindra, P. K. Shashi, *Nanotechnology* **2016**, *27*, 055701.
- [21] J.-W. Jiang, H. S. Park, *Phys. Rev. B* **2015**, *91*, 235118.
- [22] W. Zhu, M. N. Yogeesh, S. Yang, S. H. Aldave, J.-S. Kim, S. Sonde, L. Tao, N. Lu, D. Akinwande, *Nano Lett.* **2015**, *15*, 1883.
- [23] M. Ghorbani-Asl, S. Borini, A. Kuc, T. Heine, *Phys. Rev. B* **2013**, *87*, 235434.
- [24] R. Rafael, C.-G. Andrés, C. Emmanuele, G. Francisco, *J. Phys.: Condens. Matter* **2015**, *27*, 313201.
- [25] D.-Y. Khang, J. A. Rogers, H. H. Lee, *Adv. Funct. Mater.* **2009**, *19*, 1526.
- [26] W. H. Koo, S. M. Jeong, F. Araoka, K. Ishikawa, S. Nishimura, T. Toyooka, H. Takezoe, *Nat. Photonics* **2010**, *4*, 222.
- [27] W. Michael Cai, L. Juyoung, K. Pilgyu, C. Jonghyun, K. Peter, Y. Keong, N. SungWoo, *2D Mater.* **2017**, *4*, 022002.
- [28] C. An, Z. Xu, W. Shen, R. Zhang, Z. Sun, S. Tang, Y.-F. Xiao, D. Zhang, D. Sun, X. Hu, C. Hu, L. Yang, J. Liu, *ACS Nano* **2019**, *13*, 3310.
- [29] L. Li, W. Wang, P. Gong, X. Zhu, B. Deng, X. Shi, G. Gao, H. Li, T. Zhai, *Adv. Mater.* **2018**, *30*, 1706771.
- [30] H. Tian, J. Tice, R. Fei, V. Tran, X. Yan, L. Yang, H. Wang, *Nano Today* **2016**, *11*, 763.
- [31] Z. Wang, H. Jia, X.-Q. Zheng, R. Yang, G. J. Ye, X. H. Chen, P. X.-L. Feng, *Nano Lett.* **2016**, *16*, 5394.
- [32] X. Ling, S. Huang, E. H. Hasdeo, L. Liang, W. M. Parkin, Y. Tatsumi, A. R. T. Nugraha, A. A. Puzos, P. M. Das, B. G. Sumpter, D. B. Geohegan, J. Kong, R. Saito, M. Drndic, V. Meunier, M. S. Dresselhaus, *Nano Lett.* **2016**, *16*, 2260.
- [33] L. Li, P. Gong, W. Wang, B. Deng, L. Pi, J. Yu, X. Zhou, X. Shi, H. Li, T. Zhai, *ACS Nano* **2017**, *11*, 10264.
- [34] E. Liu, Y. Fu, Y. Wang, Y. Feng, H. Liu, X. Wan, W. Zhou, B. Wang, L. Shao, C.-H. Ho, Y.-S. Huang, Z. Cao, L. Wang, A. Li, J. Zeng, F. Song, X. Wang, Y. Shi, H. Yuan, Y. Hwang, H. Y. Cui, F. Miao, D. Xing, *Nat. Commun.* **2015**, *6*, 6991.



- [35] T. Low, R. Roldán, H. Wang, F. Xia, P. Avouris, L. M. Moreno, F. Guinea, *Phys. Rev. Lett.* **2014**, *113*, 106802.
- [36] H. Yuan, X. Liu, F. Afshinmanesh, W. Li, G. Xu, J. Sun, B. Lian, A. G. Curto, G. Ye, Y. Hikita, Z. Shen, S.-C. Zhang, X. Chen, M. Brongersma, H. Y. Hwang, Y. Cui, *Nat. Nanotechnol.* **2015**, *10*, 707.
- [37] Q. Guo, A. Pospischil, M. Bhuiyan, H. Jiang, H. Tian, D. Farmer, B. Deng, C. Li, S.-J. Han, H. Wang, Q. Xia, T.-P. Ma, T. Mueller, F. Xia, *Nano Lett.* **2016**, *16*, 4648.
- [38] C. Shen, Y. Liu, J. Wu, C. Xu, D. Cui, Z. Li, Q. Liu, Y. Li, Y. Wang, X. Cao, H. Kumazoe, F. Shimojo, A. Krishnamoorthy, R. K. Kalia, A. Nakano, P. D. Vashishta, M. R. Amer, A. N. Abbas, H. Wang, W. Wu, C. Zhou, *ACS Nano* **2020**, *14*, 303.
- [39] E. Zhang, P. Wang, Z. Li, H. Wang, C. Song, C. Huang, Z.-G. Chen, L. Yang, K. Zhang, S. Lu, W. Wang, S. Liu, H. Fang, X. Zhou, H. Yan, J. Zou, X. Wan, P. Zhou, W. Hu, F. Xiu, *ACS Nano* **2016**, *10*, 8067.
- [40] D. Li, H. Jussila, L. Karvonen, G. Ye, H. Lipsanen, X. Chen, Z. Sun, *Sci. Rep.* **2015**, *5*, 15899.
- [41] Y. Wang, G. Qiu, R. Wang, S. Huang, Q. Wang, Y. Liu, Y. Du, W. A. Goddard, M. J. Kim, X. Xu, P. D. Ye, W. Wu, *Nat. Electron.* **2018**, *1*, 228.
- [42] S. Deckoff-Jones, Y. Wang, H. Lin, W. Wu, J. Hu, *ACS Photonics* **2019**, *6*, 1632.
- [43] Y. Du, G. Qiu, Y. Wang, M. Si, X. Xu, W. Wu, P. D. Ye, *Nano Lett.* **2017**, *17*, 3965.
- [44] G. Qiu, C. Niu, Y. Wang, M. Si, Z. Zhang, W. Wu, P. D. Ye, *Nat. Nanotechnol.* **2019**.
- [45] Y. Wang, R. de Souza Borges Ferreira, R. Wang, G. Qiu, G. Li, Y. Qin, P. D. Ye, A. Sabbaghi, W. Wu, *Nano Energy* **2019**, *57*, 480.
- [46] W. Wu, G. Qiu, Y. Wang, R. Wang, P. Ye, *Chem. Soc. Rev.* **2018**, *47*, 7203.
- [47] Y. Xiang, J. Gao, S. R. G. Xu, W. Z. Wu, Y. S. Leng, *Nano Energy* **2019**, *58*, 202.
- [48] J. Ibers, *Nat. Chem.* **2009**, *1*, 508.
- [49] W. Wu, G. Qiu, Y. Wang, R. Wang, P. Ye, *Chem. Soc. Rev.* **2018**.
- [50] A. von Hippel, *J. Chem. Phys.* **1948**, *16*, 372.
- [51] R. Cheng, S. Jiang, Y. Chen, Y. Liu, N. Weiss, H.-C. Cheng, H. Wu, Y. Huang, X. Duan, *Nat. Commun.* **2014**, *5*, 5143.
- [52] G. Eda, G. Fanchini, M. Chhowalla, *Nat. Nanotechnol.* **2008**, *3*, 270.
- [53] W. G. Song, H.-J. Kwon, J. Park, J. Yeo, M. Kim, S. Park, S. Yun, K.-U. Kyung, C. P. Grigoropoulos, S. Kim, Y. K. Hong, *Adv. Funct. Mater.* **2016**, *26*, 2426.
- [54] Q. He, Z. Zeng, Z. Yin, H. Li, S. Wu, X. Huang, H. Zhang, *Small* **2012**, *8*, 2994.
- [55] M.-Y. Tsai, A. Tarasov, Z. R. Hesabi, H. Taghinejad, P. M. Campbell, C. A. Joiner, A. Adibi, E. M. Vogel, *ACS Appl. Mater. Interfaces* **2015**, *7*, 12850.
- [56] R. Tamalampudi, S. Y.-Y. Lu, U. R. Kumar, R. Sankar, C.-D. Liao, B. K. Moorthy, C.-H. Cheng, F. C. Chou, Y.-T. Chen, *Nano Lett.* **2014**, *14*, 2800.
- [57] Q. Wang, K. Xu, Z. Wang, F. Wang, Y. Huang, M. Safdar, X. Zhan, F. Wang, Z. Cheng, J. He, *Nano Lett.* **2015**, *15*, 1183.
- [58] Y. Zhou, Y. Nie, Y. Liu, K. Yan, J. Hong, C. Jin, Y. Zhou, J. Yin, Z. Liu, H. Peng, *ACS Nano* **2014**, *8*, 1485.
- [59] H. Liu, A. T. Neal, Z. Zhu, Z. Luo, X. Xu, D. Tománek, P. D. Ye, *ACS Nano* **2014**, *8*, 4033.
- [60] K. S. Novoselov, A. K. Geim, S. V. Morozov, D. Jiang, Y. Zhang, S. V. Dubonos, I. V. Grigorieva, A. A. Firsov, *Science* **2004**, *306*, 666.
- [61] Y. Liu, W. Wu, W. A. Goddard, *J. Am. Chem. Soc.* **2018**, *140*, 550.
- [62] P. J. Brown, J. B. Forsyth, *Acta Crystallogr. A* **1996**, *52*, 408.
- [63] R. Frisenda, Y. Niu, P. Gant, A. J. Molina-Mendoza, R. Schmidt, R. Bratschitsch, J. Liu, L. Fu, D. Dumcenco, A. Kis, D. P. De Lara, A. Castellanos-Gomez, *J. Phys. D: Appl. Phys.* **2017**, *50*, 074002.
- [64] J. Kang, V. K. Sangwan, J. D. Wood, M. C. Hersam, *Acc. Chem. Res.* **2017**, *50*, 943.
- [65] C. Tan, H. Zhang, *Nat. Commun.* **2015**, *6*, 7873.
- [66] X. Zhang, Y. Xie, *Chem. Soc. Rev.* **2013**, *42*, 8187.
- [67] Z. Liu, S. Li, Y. Yang, Z. Hu, S. Peng, J. Liang, Y. Qian, *New J. Chem.* **2003**, *27*, 1748.
- [68] S. A. Awad, *Electrochim. Acta* **1962**, *7*, 677.
- [69] J. Song, H. Jiang, Z. J. Liu, D. Y. Khang, Y. Huang, J. A. Rogers, C. Lu, C. G. Koh, *Int. J. Solids Struct.* **2008**, *45*, 3107.
- [70] A. J. Baca, J.-H. Ahn, Y. Sun, M. A. Meitl, E. Menard, H.-S. Kim, W. M. Choi, D.-H. Kim, Y. Huang, J. A. Rogers, *Angew. Chem., Int. Ed.* **2008**, *47*, 5524.
- [71] I. D. Johnston, D. K. McCluskey, C. K. L. Tan, M. C. Tracey, *J. Micromech. Microeng.* **2014**, *24*, 035017.
- [72] K. Khanafer, A. Duprey, M. Schlicht, R. Berguer, *Biomed. Microdevices* **2009**, *11*, 503.
- [73] N. Iguñiz, R. Frisenda, R. Bratschitsch, A. Castellanos-Gomez, *Adv. Mater.* **2019**, *31*, 1807150.
- [74] H. Gercek, *Int. J. Rock Mech. Min. Sci.* **2007**, *44*, 1.
- [75] P. W. Bridgman, *Phys. Rev.* **1917**, *9*, 138.
- [76] Y. Wang, Y. Chen, H. Li, X. Li, H. Chen, H. Su, Y. Lin, Y. Xu, G. Song, X. Feng, *ACS Nano* **2016**, *10*, 8199.
- [77] Y. Du, G. Qiu, Y. Wang, M. Si, X. Xu, W. Wu, P. D. Ye, *Nano Lett.* **2017**, *17*, 3965.
- [78] A. Pine, G. Dresselhaus, *Phys. Rev. B* **1971**, *4*, 356.
- [79] B. Torrie, *Solid State Commun.* **1970**, *8*, 1899.
- [80] Q. Wang, M. Safdar, K. Xu, M. Mirza, Z. Wang, J. He, *ACS Nano* **2014**, *8*, 7497.
- [81] A. Jain, P. Bharadwaj, S. Heeg, M. Parzefall, T. Taniguchi, K. Watanabe, L. Novotny, *Nanotechnology* **2018**, *29*, 265203.
- [82] N. Reitzel, D. R. Greve, K. Kjaer, P. B. Howes, M. Jayaraman, S. Savoy, R. D. McCullough, J. T. McDevitt, T. Bjørnholm, *J. Am. Chem. Soc.* **2000**, *122*, 5788.
- [83] B. G. Shin, G. H. Han, S. J. Yun, H. M. Oh, J. J. Bae, Y. J. Song, C.-Y. Park, Y. H. Lee, *Adv. Mater.* **2016**, *28*, 9378.
- [84] Q. Zheng, W. H. Ip, X. Lin, N. Yousefi, K. K. Yeung, Z. Li, J.-K. Kim, *ACS Nano* **2011**, *5*, 6039.
- [85] P. Anees, M. C. Valsakumar, B. K. Panigrahi, *Phys. Chem. Chem. Phys.* **2016**, *18*, 2672.
- [86] J. Qiu, Q. Jiang, *J. Appl. Phys.* **2007**, *102*, 074101.
- [87] P. Kang, M. C. Wang, P. M. Knapp, S. Nam, *Adv. Mater.* **2016**, *28*, 4639.
- [88] A. S. Pine, G. Dresselhaus, *Phys. Rev. B* **1971**, *4*, 356.
- [89] S. Tutilhasi, G. G. Roberts, R. C. Keezer, R. E. Drews, *Phys. Rev.* **1969**, *177*, 1143.
- [90] Z. Zhang, L. Li, J. Horng, N. Z. Wang, F. Yang, Y. Yu, Y. Zhang, G. Chen, K. Watanabe, T. Taniguchi, X. H. Chen, F. Wang, Y. Zhang, *Nano Lett.* **2017**, *17*, 6097.
- [91] W. Wu, Y. Wei, L. Wang, Z. Wang, *Adv. Mater.* **2010**, *22*, 4711.
- [92] G. Kresse, D. Joubert, *Phys. Rev. B* **1999**, *59*, 1758.
- [93] G. Kresse, J. Furthmüller, *Comput. Mater. Sci.* **1996**, *6*, 15.
- [94] G. Kresse, J. Furthmüller, *Phys. Rev. B* **1996**, *54*, 11169.
- [95] J. Klimeš, D. R. Bowler, A. Michaelides, *J. Phys.: Condens. Matter* **2009**, *22*, 022201.